AIAA JOURNAL
Vol. 41, No. 12, December 2003

Numerical Simulation of Vectoring of a Primary Jet with a Synthetic Jet

Dahai Guo,* Andrew W. Cary,† and Ramesh K. Agarwal‡
Washington University, St. Louis, Missouri 63130

The vectoring control of a primary jet with an averaged-zero-mass-flux synthetic jet is simulated using the two-dimensional Reynolds-averaged Navier–Stokes equations. The numerical results show the general agreement with the experiments. The vectoring effects of some parameters of the synthetic jet, such as the location, oscillating frequency, and velocity amplitude, are studied at two angles (0 and 60 deg) of the synthetic jet. The simulations show that in a certain range of velocity for the primary jet there exist optimal values for these parameters respectively, where the largest vectoring angle of the primary jet can be achieved with other parameters fixed. In addition, the synthetic jet can result in a much larger vectoring angle and vectoring force for the primary jet at 60 deg than that at 0 deg. It is hypothesized that the vectoring of a primary jet with a synthetic jet is mainly a combined effect of the local lower pressure and resistance caused by the synthetic jet.

Nomenclature

C_p = pressure coefficient, $(p - p_\infty)/0.5\rho U_{\text{ave}}^2$
d_{pull} = distance between the synthetic jet and the primary jet
d^* = d_{pull}/h
f = oscillating frequency of the synthetic jet
f_c = characteristic frequency of the primary jet, U_{ave}/H
f^* = f/f_c
H = width of the primary jet
h = width of the orifice of the synthetic jet
L_o = stroke length,

$$\int_0^\tau u_o(t)\,\mathrm{d}t$$

Re_{U_o} = Reynolds number based on average orifice velocity, $\rho U_o h/\mu$
T = period of the harmonic motion
t = time
t^* = t/T
U_{amp} = cross-stream averaged streamwise velocity amplitude at the exit of the orifice
U_{ave} = cross-stream averaged velocity of the primary jet
U_o = average orifice velocity, L_o/T
$\boldsymbol{u}$ = velocity vector
u_o = streamwise velocity at exit plane of orifice
v_o = cross-stream velocity at exit plane of orifice
x = streamwise coordinate
y = cross-stream coordinate
α = vectoring angle of the primary jet
θ = angle of the synthetic jet
λ = $U_{\text{amp}}/U_{\text{ave}}$
λ^{-1} = $U_{\text{ave}}/U_{\text{amp}}$
μ = molecular viscosity
μ_t = turbulent viscosity
ρ = density
τ = time of discharge, $T/2$
ω = angular frequency
ω_z = vorticity, nondimensionalized by U_o and h

Introduction

SYNTHETIC jet actuators[1] can be used to control shear flows effectively, which has been demonstrated by Smith and Glezer.[2] The synthetic jet is created by entraining the surrounding fluid. It has an attractive nature of zero-net-mass injection, but the momentum is impulsed into the external flow. Therefore small-scale motion is enhanced, and the local instability of the flow is excited. A variety of flow control results have been achieved using synthetic jets, including thrust vectoring,[1–4] mixing enhancement,[5] and separation control.[6]

Smith and Glezer[1] have studied the flow behavior of a rectangular synthetic jet actuator, whose exit orifice is 0.5 mm wide and 75 mm long. One side of a cavity is driven by a piezoelectric diaphragm in a periodic manner such that the fluid in the surrounding environment enters and exits the cavity. It needs only mechanical or electrical power, but no fluid from other sources. Figure 1 illustrates the cross section of an actuator operating in still air. As the fluid is driven out of the cavity in the blowing stroke, a shear layer is formed between the expelled fluid and the surrounding fluid because of their velocity difference. At the end of the blowing stroke, this layer of the vorticity rolls up and forms a vortex pair. In the suction stroke the fluid in the surrounding environment is entrained into the cavity. At that time, however, the vortex pair generated during the blowing stroke has moved far enough away, and it is not ingested back into the cavity. Thus a train of vortex pairs is created by the actuator. Although no mass flux is out of the cavity in the time-average sense, the momentum impulsed into the external flow is nonzero in each period. Flow visualization (Fig. 1) indicates that the train of vortex pairs breaks down into a turbulent jet near the orifice. On the average value the streamwise velocity profile appears similar to a steady jet.

Synthetic jets provide an alternate effective approach to control the aerodynamics of a propulsive jet that emanates from a nozzle. Synthetic jet actuators are attractive for shear flow control because they have no moving parts, can produce a controllable excitation, and can be easily integrated into a functioning device. There have been many investigations regarding vectoring of a primary jet emanating from a nozzle using fluidic synthetic jet control. Recent investigations include the studies by Smith and Glezer,[2] Pack and Seifert,[7] Miller et al.,[8] Raman,[9] and Strykowski et al.[10] In the experiments of Smith and Glezer,[2] a millimeter-scale actuator jet is placed near the exit plane of a high-aspect-ratio primary jet and nominally collinear with it, which is denoted as pull mode in Fig. 2. The synthetic jet induces strong entrainment of ambient fluid and leads to the vectoring of a primary jet at angles of the order of 30 deg.

Received 31 December 2001; presented as Paper 2002-3284 at the AIAA 1st Flow Control Conference, St. Louis, MO, 24–27 June 2002; revision received 8 June 2003; accepted for publication 30 June 2003.

*Graduate Research Assistant, Department of Mechanical Engineering. Member AIAA.

†Adjunct Professor, Department of Mechanical Engineering. Senior Member AIAA.

‡William Palm Professor, Department of Mechanical Engineering. Fellow AIAA.

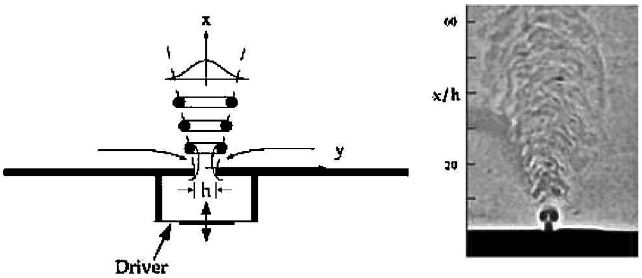

Fig. 1 Schematic of a synthetic jet actuator and schlieren flow visualization from the experiments of Smith and Glezer.[1]

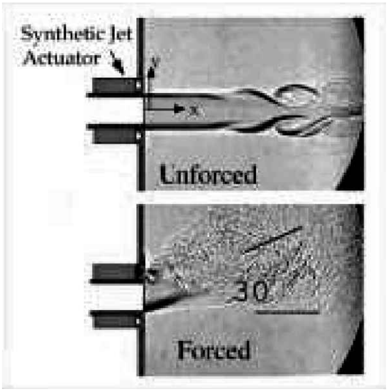

Fig. 2 Schlieren flow visualization of the vectoring of a primary jet from the experiments of Smith and Glezer.[2]

The complex nature of an isolated and adjacent twin synthetic jet actuators has previously been modeled by Kral et al.,[11] Kral and Guo,[12] and Guo et al.[13] A simplified boundary condition for the synthetic jet is implemented in the framework of the Reynolds-averaged Navier–Stokes (RANS) equations. This approach can yield efficient approximate solutions for practical engineering applications. Using two-dimensional simulations, good agreement with the experiments of Smith and Glezer[2] is observed for the mean jet similarity profiles. Later, Kral and Guo[12] capture the vectoring of a primary jet in the push/pull modes in their numerical simulations using the experimental conditions of Smith and Glezer.[2] Guo and Cary[14] extend the work of Kral and Guo and show that the numerical simulations match quite well with the experiments of Smith and Glezer.[2]

In this paper simulations are performed for vectoring control of a primary jet with a synthetic jet in the pull mode. The vectoring effects of some of the parameters of the synthetic jet are discussed, such as the distance from the primary jet, velocity amplitude, oscillating frequency, and the angle. The optimal values of these parameters are estimated to achieve the maximum vectoring benefit. Finally, a hypothesis to explain the vectoring of the primary jet with the sythetic jet is postulated based on the simulation results.

Governing Equations

The incompressible flow solver, INS2D, developed by Rogers and Kwak[15] and Rogers et al.,[16] is employed in the simulations. The two-dimensional incompressible unsteady RANS equations are solved.

The governing equations are the conservation of mass and momentum given by the continuity equation

$$\nabla \cdot \bar{\boldsymbol{u}} = 0 \tag{1}$$

and the Reynolds-averaged Navier–Stokes equations

$$\rho \frac{\partial \bar{\boldsymbol{u}}}{\partial t} + \rho \bar{\boldsymbol{u}} \cdot \nabla \bar{\boldsymbol{u}} = -\nabla \bar{p} + \nabla \cdot (\mu + \mu_t) \nabla \bar{\boldsymbol{u}} \tag{2}$$

where the overbar represents a Reynolds-averaged quantity. The equations are solved in a time-accurate manner using the method of pseudocompressibility. With this method subiterations are required to satisfy the conservation of mass at each time step. An upwind differencing scheme based on flux-difference splitting is used to compute the convective terms using a fifth-order differencing scheme. The viscous fluxes are differenced with a second-order accurate central-difference scheme. The equations are solved by employing a generalized minimum residual method.[17] This solution procedure is stable and capable of running at large time steps in pseudotime, leading to rapid convergence for each physical time step.

Actuator Modeling

The synthetic jet actuator introduces periodic momentum inputs by oscillating the flow within a cavity. To model the perturbation on the flow caused by the harmonic forcing of the actuator, a suction/blowing-type boundary condition is developed by Kral et al.,[11] which guarantees zero-net-mass induction in the time-average sense. The perturbation to the flowfield is introduced through the wall-normal component of velocity at the bottom of the cavity of the synthetic jet, which uses a "top-hat" velocity distribution

$$\bar{u}(x = 0, y, t) = U_A \sin(\omega t + \phi) \tag{3}$$

$$\bar{v}(x = 0, y, t) = 0 \tag{4}$$

where $\bar{u}$ is the streamwise component of velocity and $\bar{v}$ is the cross-stream component of velocity. U_A is the amplitude of the synthetic jet velocity at the bottom of the cavity, and it satisfies $U_A h_c = U_{\text{amp}} h$, where h_c is the width of the cavity.

A modified boundary condition on the wall pressure at the orifice is also introduced. The typical boundary condition on the pressure at a solid surface is

$$\frac{\partial \bar{p}}{\partial x} = 0 \tag{5}$$

This condition results by considering the component of the momentum equation normal to the jet, ignoring viscous effects. At the boundary of the synthetic jet, however, the time-harmonic normal velocity perturbation is taken into account, and the modified boundary condition for the pressure becomes

$$\frac{\partial \bar{p}}{\partial x} = -\rho \frac{\partial \bar{u}}{\partial t} \tag{6}$$

The Spalart–Allmaras[18] one-equation turbulence model (denoted as SA) is employed to close the system of equations. The model solves a single transport equation for a modified turbulent viscosity. Figure 3 shows the grid employed in the computations.

Results and Analysis

Comparisons with the Experiments

The computational parameters employed in the simulations are those used in the experiments of Smith and Glezer.[2] The width of the

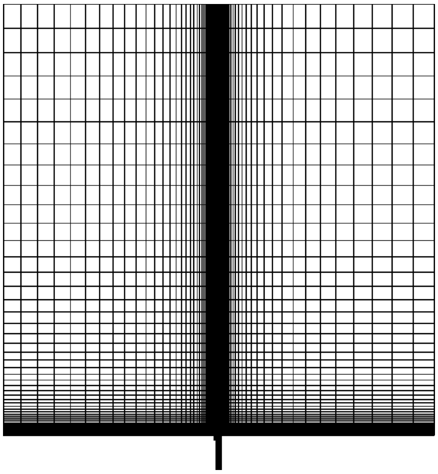

Fig. 3 Computational grid (41 × 72 for the duct, 31 × 51 for the cavity, 201 × 101 for the external domain).

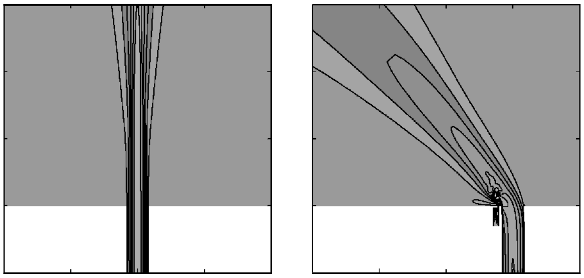

a) Unforced primary jet **b) Forced primary jet**

Fig. 4 Contours of the magnitude of time-averaged velocity for $Re_{U_o} = 383$.

primary jet $H = 12.7$ mm, the width of the synthetic jet $h = 0.5$ mm, and $d_{\text{pull}} = 3.556h$, which is the distance between the synthetic jet and the primary jet. The oscillation frequency of the synthetic jet is 1120 Hz.

Figure 4 shows the contours of the magnitude of time-averaged velocity of the primary jet. The velocity amplitude of the synthetic jet is 37.83 m/s, the associated Reynolds number is $Re_{U_o} = 383$, and the cross-stream averaged velocity of the primary jet is $U_{\text{ave}} = 5.16$ m/s. The unforced primary jet is symmetric about the centerline. The vectoring angle of the forced primary jet is of the same order as in the experiment shown in Fig. 2.

The temporal evolution of the vorticity near the exits of the jets in the pull mode is depicted in Fig. 5 for $Re_{U_o} = 314$. The first column is from the experiment of Smith et al., and the second column is the numerical simulation. The main vortex structures in the numerical results are similar to those in the experiment. The vortex pair generated by the synthetic jet merges into the primary jet. During the suction stroke, the synthetic jet entrains some fluid from the primary jet and enhances the strength of the vortex in the small gap between them. At the beginning of the next blowing stroke, the vortex is attached to the boundary layer between the primary and synthetic jets, whose vorticity becomes negative at this time. During the first half of the blowing stroke, the boundary layer changes direction and separates the vortex from the wall. This vortex then interacts with the vortices from the synthetic jet and the flow of the primary jet, dissipates very quickly, and merges into the primary jet. Compared with the experiment, the boundary layer in the simulations is thinner, and the strength of the vortex between the primary and synthetic jets is weaker. This might be caused by the large dissipation in the SA turblulence model.

Effect of Various Parameters on Vectoring

Figure 6 shows the schematic near the exits of the synthetic jet and the primary jet. The angle θ is defined as the angle between the normal to the external flow boundary and the orifice wall of the synthetic jet. The width of the orifice is fixed in all of the simulations, that is, $h = 0.5$ mm.

The boundaries of the primary jet can be approximated as curves on which the magnitude of the time-averaged velocity is equal to $0.05 * V_{\max}$, where $V_{\max}$ represents the maximum value of the magnitude of the velocity at different distances from the wall. This schematic is shown in Fig. 7. The curve on which the velocity magnitude reaches maximum at different distances from the wall matches well with the line, which is obtained from those points on the curve with linear regression. Because the regression line is around the middle of the two outer boundaries of the primary jet, the vectoring angle of the primary jet can be defined as the angle α between the regression line of the points, where velocity magnitude of the primary jet becomes maximum and the central line of the nozzle of the primary jet. This definition of the vectoring angle is employed in the rest of the paper.

The location, frequency, velocity amplitude, and angle of the synthetic jet are important parameters that affect the vectoring angle α of the primary jet. In the following sections the influence of these parameters is discussed in detail, in which d^* keeps 3.556 except when the effect of the location is studied.

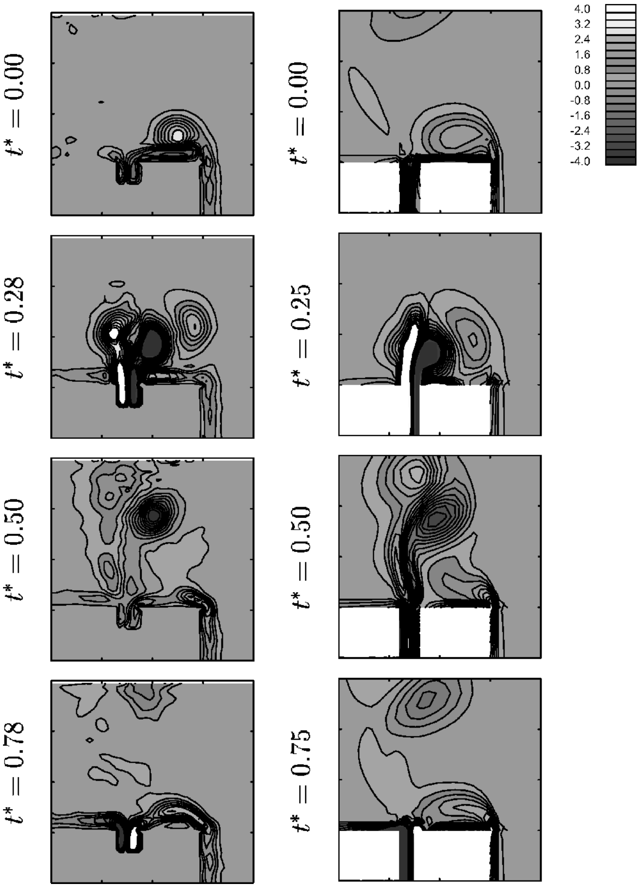

a) **b)**

Fig. 5 Temporal evolution of vorticity near the exit of the jets for the pull mode: a) experiment of Smith and Glezer[19] and b) the numerical simulation.

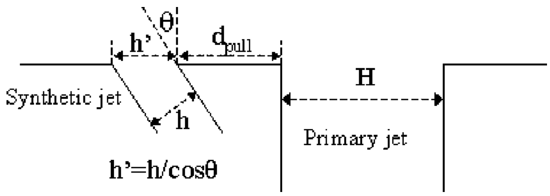

Fig. 6 Schematic of the synthetic jet at an angle.

$\theta = 0$ deg

To study the vectoring effect of the location of the synthetic jet, a number of simulations are considered, with d^* varying from 1.0 to 5.0. Figure 8 shows the variation of the vectoring angle α with the distance d^*. The vectoring angle α is about 7.8 deg when d^* is 1.0. When d^* is between 1.0 and 4.0, α increases gradually as d^* increases. The angle α reaches a maximum of 31.9 deg when $d^* = 4.0$. For $d^* > 4.0$, α decreases rapidly, and for $d^* = 5.0$, α is reduced to 14.7 deg.

Simulations with different frequencies of the synthetic jet are then considered to study its effect on the vectoring of the primary jet. Other parameters are fixed, such as $Re_{U_o} = 383$ and $U_{\text{ave}} = 7.0$ m/s. The characteristic frequency of the primary jet f_c is defined as U_{ave}/H. Here, $f_c = 7.0/0.0127 = 551.18$ Hz. The nondimensional frequency f^* is defined as f/f_c.

Figure 9 shows the variation of the vectoring angle of the primary jet for various frequencies of the synthetic jet. When $0.91 \le f^* \le 1.81$, the vectoring angle increases rapidly from 14.4 to 30.0 deg, and for $f^* > 1.81$ it decreases to 14.6 deg as $f^* = 3.62$. The vectoring angle reaches a maximum value of 30.0 deg when f^* is about 1.81.

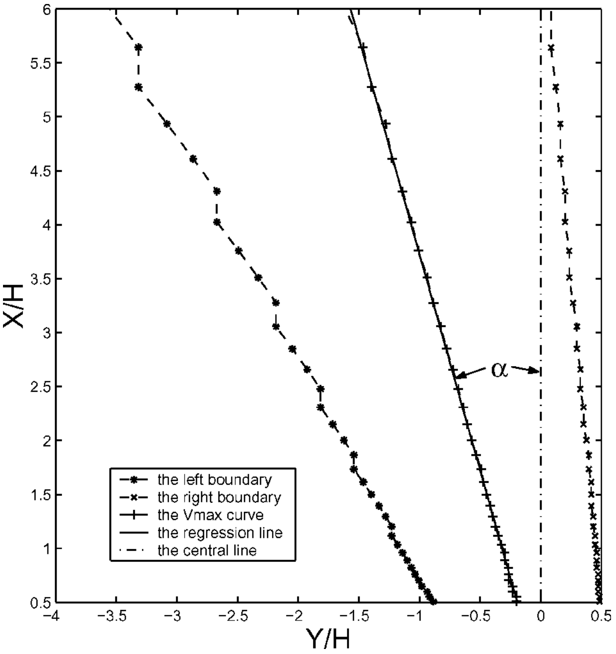

Fig. 7 Schematic representation of the vectoring angle of the primary jet.

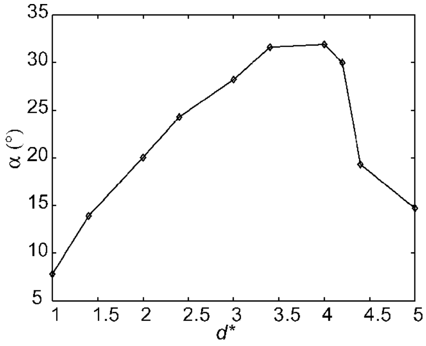

Fig. 8 Variation of the vectoring angle of the primary jet with the distance d^* (Re_{U_o} = 383, U_{ave} = 7 m/s, and f = 1120 Hz).

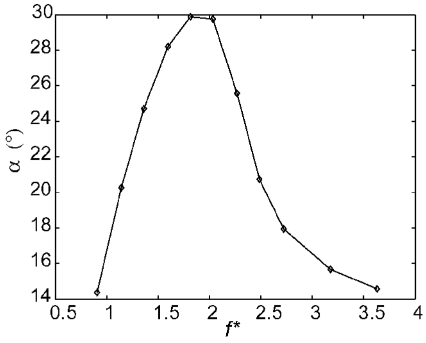

Fig. 9 Variation of the vectoring angle of the primary jet with frequency f^* (Re_{U_o} = 383 and U_{ave} = 7 m/s).

The velocity amplitude of the synthetic jet is the third parameter to study, and its effect on the vectoring angle of the primary jet is shown in Fig. 10, where $f = 1120$ Hz, $U_{\text{ave}} = 7.0$ m/s, and $d_{\text{pull}} = 3.556h$. When $\lambda < 7.0$, the vectoring angle increases as λ increases. When $\lambda = 7.0$, the vectoring angle of the primary jet is the largest: $\alpha_{\max} = 31.0$ deg. For $\lambda > 7.0$, however, the vectoring angle decreases gradually.

Figure 11 shows the variation of the vectoring angle of the primary jet with the velocity of the primary jet. The parameters of the synthetic jet are fixed, that is, $f = 1120$ Hz and $Re_{U_o} = 383$. With increasing velocity of the primary jet, the vectoring angle becomes smaller. When λ^{-1} is 0.132 ($U_{\text{ave}} = 5.0$ m/s), the vectoring angle is about 37.4 deg. When λ^{-1} is 0.244 ($U_{\text{ave}} = 13.0$ m/s), however, the vectoring angle is just 10.0 deg.

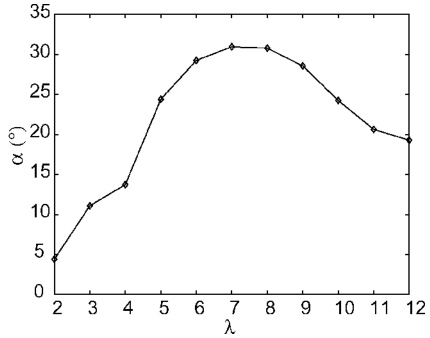

Fig. 10 Variation of the vectoring angle of the primary jet with λ (f = 1120 Hz and U_{ave} = 7.0 m/s).

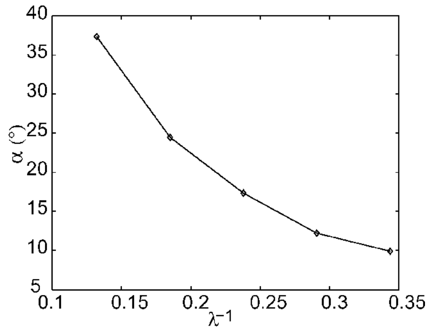

Fig. 11 Variation of the vectoring angle of the primary jet with λ^{-1} (f = 1120 Hz and Re_{U_o} = 383).

θ = 60 deg

In all of the preceding simulations, the angle of the synthetic jet θ is zero. Here we discuss the vectoring effect of velocity amplitude U_{amp} and frequency f of the synthetic jet at $\theta = 60$ deg.

Vectoring effect of the velocity amplitude U_{amp} of the synthetic jet at $\theta = 60$ deg is first studied with $\lambda = 3.0 \sim 6.0$, $f = 1120$ Hz, and $U_{\text{ave}} = 7.0$ m/s. Figure 12 shows the variation of the vectoring angle of the primary jet with the velocity amplitude of the synthetic jet at $\theta = 60$ deg. α increases rapidly from 13.7 to 87 deg when λ increases from 3.0 to 5.0. For $\alpha > 85$ deg, the primary jet attaches to the wall. Figure 13 clearly shows that the primary jet is attached to the wall in the case $\lambda = 6.0$. Figure 14 shows that the time-averaged pressure coefficient is much lower near the exit of the primary jet and the synthetic jet. This is strongly related to the vectoring of the primary jet. It is interesting to note from Fig. 10 that at $\theta = 0$ deg, there is an optimal velocity amplitude of the synthetic jet, at which a maximum vectoring of 31.0 deg is obtained, and the primary jet cannot be attached to the wall.

The temporal evolution of vorticity contours in Fig. 15 shows that a vortex with positive vorticity is generated between the synthetic jet and the primary jet. Although its strength changes with time in an oscillating period of the synthetic jet, it does not separate from the wall. In the suction stroke some fluid of the primary jet is entrained into the synthetic jet along with some fluid from the surrounding environment. The blowing stroke of the synthetic jet generates a vortex pair, which travels away from the jets along the exit plane.

Now we discuss the effect of the frequency of the synthetic jet at $\theta = 60$ deg on the vectoring of the primary jet. The oscillating frequency of the synthetic jet f^* varies from 0.23 to 3.63. Other flow parameters are fixed, that is, $f_c = 551.18$ Hz, $U_{\text{amp}} = 30.0$ m/s, and $U_{\text{ave}} = 7.0$ m/s.

Figure 16 shows the variation of the vectoring angle of the primary jet α with the frequency f^* at $\theta = 60$ deg. When f^* varies from 0.23 to 0.91, α increases sharply from 32.0 deg to about 88.5 deg.

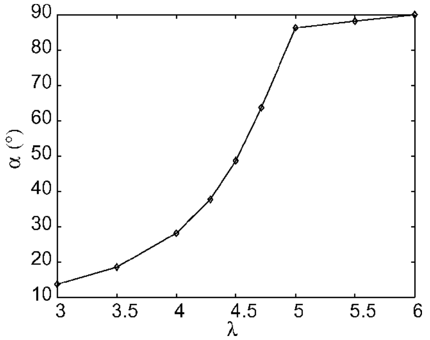

Fig. 12 Variation of the vectoring angle of the primary jet with U_{amp} at θ = 60 deg (U_{ave} = 7.0 m/s and f = 1120 Hz).

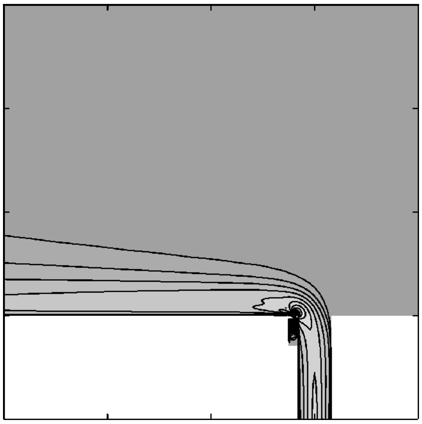

Fig. 13 Magnitude of time-averaged velocity for λ = 6.0 at θ = 60 deg (f = 1120 Hz and U_{ave} = 7.0 m/s).

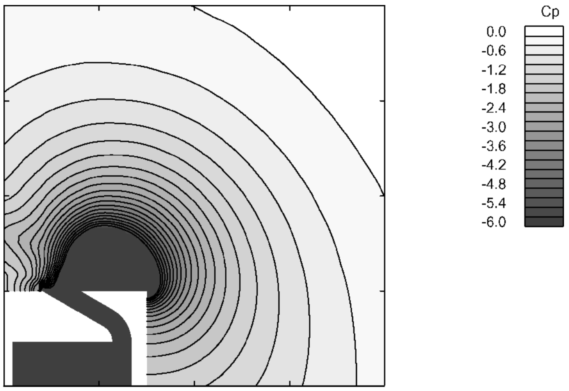

Fig. 14 Contour of time-averaged pressure coefficient for λ = 6.0 at θ = 60 deg (f = 1120 Hz and U_{ave} = 7.0 m/s).

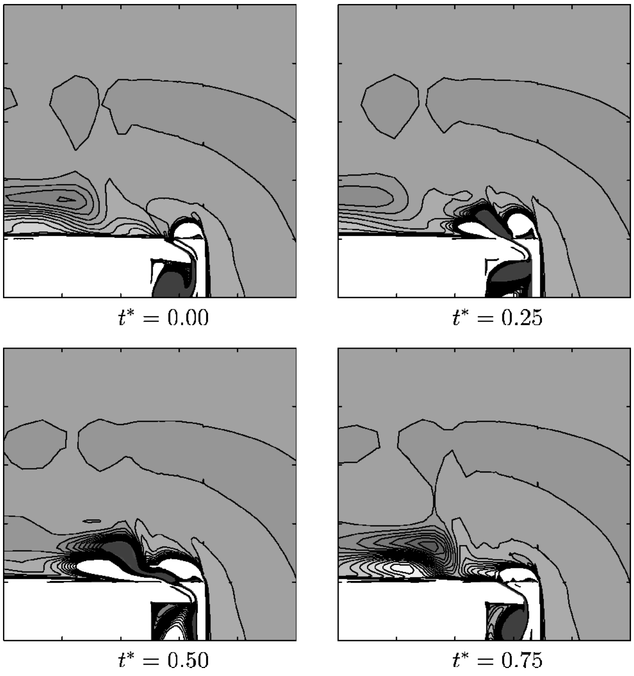

Fig. 15 Temporal evolution of vorticity contours around the jets for λ = 6.0 at θ = 60 deg (f = 1120 Hz and U_{ave} = 7.0 m/s).

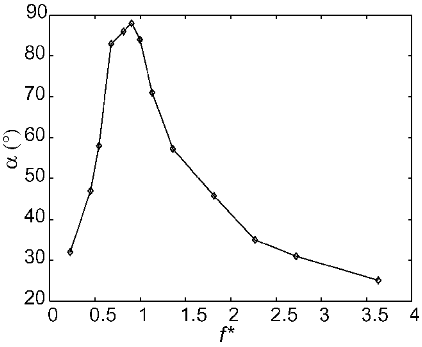

Fig. 16 Variation of the vectoring angle of the primary jet with the frequency f^* at θ = 60 deg (U_{ave} = 7.0 m/s and U_{amp} = 30.0 m/s).

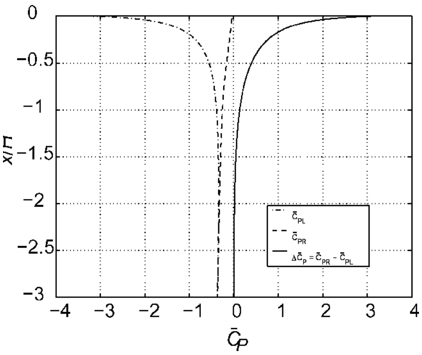

Fig. 17 Time-averaged pressure coefficients along the walls of the nozzle of the primary jet (Re_{U_o} = 496, U_{ave} = 7.0 m/s, and f = 1120 Hz).

When $f^* > 0.91$, α reduces gradually with increase in frequency. When $f^* = 3.63$, $\alpha \approx 25.1$ deg. As shown in Fig. 9, there exists an optimal frequency $f^* = 1.81$ of the synthetic jet at $\theta = 0$ deg for the largest vectoring angle of 30 deg. However, the optimal frequency at $\theta = 60$ deg is about 0.91, where the primary jet is already attached to the wall.

Vectoring Force $\bar{F}^*$

The time-averaged pressure coefficient along the two walls of the nozzle of the primary jet is shown in Fig. 17. When it is closer to the exit of the nozzle, the time-averaged pressure along the left wall $\bar{C}_{p_L}$ decreases rapidly and that on the right wall $\bar{C}_{p_R}$ increases slowly. When $x/H < -2.0$, the pressures along the two walls are the same. When $x/H > -2.0$, the pressures become different; the pressure along the wall closer to the synthetic jet is smaller than that along the other wall. The pressure difference $\Delta\bar{C}_p = \bar{C}_{p_R} - \bar{C}_{p_L}$ along the two walls becomes larger when it is closer to the exit of the jet, and most of the contribution to the pressure difference occurs within $-1.0 < x/H < 0.0$. At the exit of the primary jet, $\Delta\bar{C}_p$ achieves a maximum, which is about 3.0.

The nondimensional force caused by the pressure difference between the two walls of the nozzle of the primary jet is defined as follows:

$$F^* = \int_o^L \Delta C_p \, \mathrm{d}x/H \tag{7}$$

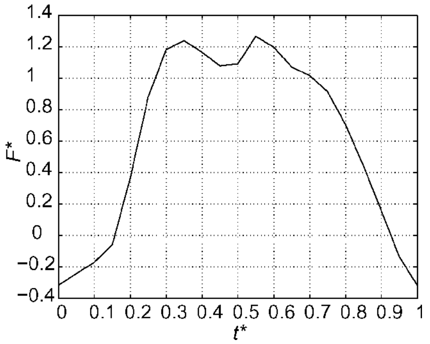

a) θ = 0 deg and Re_{U_o} = 496

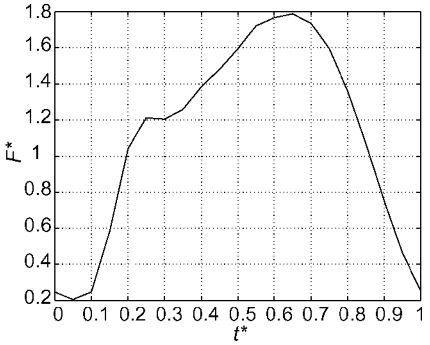

b) θ = 60 deg and Re_{U_o} = 535

Fig. 18 Temporal evolution of force F^* in one oscillation period (U_{ave} = 7.0 m/s and f = 1120 Hz).

where L is the length of the nozzle. Figures 18a and 18b show the temporal evolutions of the force F^* in one oscillation period of the synthetic jet for $\theta = 0$ and 60 deg, respectively. A large unsteadiness in the force is demonstrated in the two cases. Generally, the vectoring force F^* increases in the blowing stroke and then decreases in the suction stroke. However, the figures clearly show that $\theta = 60$ deg can get larger vectoring force in the whole oscillating period. For the case $\theta = 0$ deg, F^* is negative at the beginning of the blowing stroke and at the end of the suction stroke, which suggests that the pressure along the wall closer to the synthetic jet is sometimes even higher than that along the other wall.

The time-averaged force is defined as

$$\bar{F}^* = \int_0^T F^* \mathrm{d}t/T$$

Figure 19 shows the variation of $\bar{F}^*$ with λ at $\theta = 0$ and 60 deg, where $U_{\text{ave}} = 7.0$ m/s and $f = 1120$ Hz for both angles θ. At $\theta = 0$ deg, $\bar{F}^*$ increases from 0.07 to 0.64 as λ changes from 2.0 to 7.0. When $\lambda > 7.0$, $\bar{F}^*$ changes a little, and $\bar{F}^* \approx 0.65$ when $\lambda = 10.0$. But at $\theta = 60$ deg, $\bar{F}^*$ increases rapidly from 0.30 to 1.00 as λ changes from 3.0 to 5.0. When $\lambda = 8.0$, $\bar{F}^* \approx 1.15$, which is much larger than the force (0.65) at $\theta = 0$ deg.

Figure 20 shows the variation of $\bar{F}^*$ with f^* at $\theta = 0$ and 60 deg, where $U_{\text{ave}} = 7.0$ m/s. Although Re_{U_o} at $\theta = 60$ deg is smaller than that at $\theta = 0$ deg with the same frequency, $\theta = 60$ deg always obtains larger $\bar{F}^*$ than $\theta = 0$ deg. At $\theta = 60$ deg, $\bar{F}^*_{\max} \approx 0.88$ at $f^* \approx 1.00$. However, at $\theta = 0$ deg, $\bar{F}^*_{\max}$ is about 0.57, where $f^* \approx 2.03$.

These figures clearly show that $\theta = 60$ deg generates much larger vectoring force than $\theta = 0$ deg with the same or even less input power. The results again show that a synthetic jet at $\theta = 60$ deg can provide greater vectoring benefit than at smaller value of θ.

Vectoring Hypothesis

If the distance between the synthetic jet and the primary jet d_{pull} is too large, the synthetic jet has no vectoring effect on the primary jet because they have no interaction. If it is too small, on the other hand, the momentum of the synthetic jet provides stronger resistance to the vectoring of the primary jet when the angle of the synthetic jet is not bigger than zero, although it causes larger local flow unsteadiness. Therefore, there should be an optimal distance between the synthetic jet and the primary jet, from which the largest vectoring benefit can be obtained.

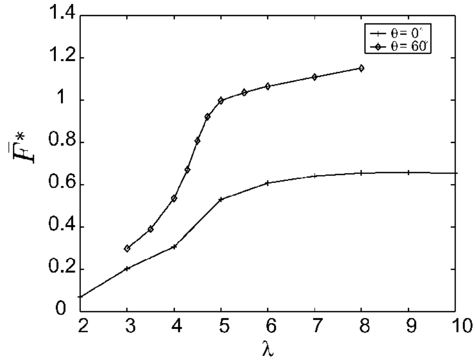

Fig. 19 Variation of the vectoring force $\bar{F}^*$ with λ at θ = 0 and 60 deg (U_{ave} = 7.0 m/s and f = 1120 Hz).

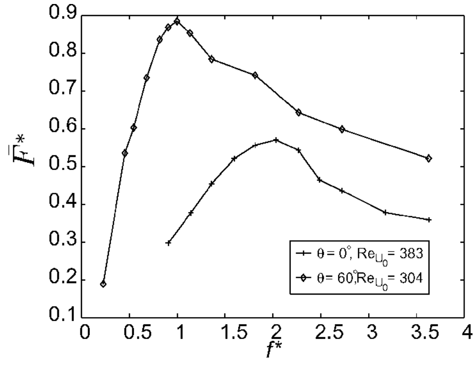

Fig. 20 Variation of the vectoring force $\bar{F}^*$ with f^* at θ = 0 and 60 deg (U_{ave} = 7.0 m/s and f = 1120 Hz).

There are two characteristic parameters of the synthetic jet that affect the interaction between the synthetic jet and the external flow. They are as follows: 1) the stroke length

$$L_o = \int_0^\tau u_o(t)\,\mathrm{d}t$$

where $\tau = T/2$, which was introduced by Smith and Glezer[19]; 2) the local acceleration at the exit of the synthetic jet $a_0 = \partial u_o/\partial t$. L_o is the downstream distance needed for the development of the synthetic jet in the blowing stroke, which is related to the size of the area affected by the synthetic jet; a_0, on the other hand, is strongly related to pressure around it. Because $u_o = U_{\text{amp}} \sin(2\pi f t)$ in the simulations, $L_o = U_{\text{amp}}/\pi f$ and $a_0 = a_{0_{\max}} \cos(2\pi f t)$, where $a_{0_{\max}} = 2\pi f U_{\text{amp}}$.

It is clear that as f increases, L_o decreases, and $a_{0_{\max}}$ increases, which means that the size of the domain affected by the synthetic jet is smaller with lower pressure, because with higher $a_{0_{\max}}$ the shear stress between the synthetic jet and the surrounding fluid is larger. With the combined effects of these two characteristics of the synthetic jet, there exists an optimal frequency for obtaining the largest vectoring benefit. In addition, when U_{amp} increases both L_o and $a_{0_{\max}}$ increase, which means that the size of the lower pressure region is larger. However, higher U_{amp} also means larger resistance of momentum of the synthetic jet to the vectoring of the primary jet. Therefore, there also exists an optimal U_{amp} from which the largest vectoring angle of the primary jet is obtained with other parameters fixed.

The synthetic jet injects the momentum M into the external flow in the blowing stroke. The momentum M not only causes the local unsteadiness but also resists the vectoring of the primary jet. Figure 21 shows a schematic of the momentum components of the synthetic jet in the blowing stroke, where M_x is the streamwise momentum component and M_y is the cross-stream momentum component.

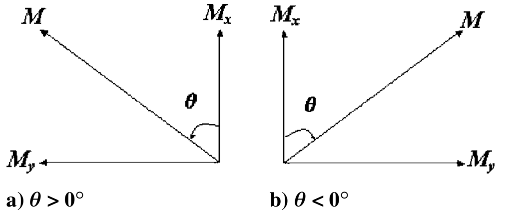

a) $\theta > 0°$ b) $\theta < 0°$

Fig. 21 Schematic of the momentum components of the synthetic jet in the blowing stroke.

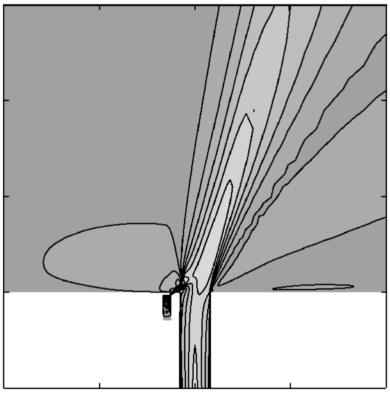

Fig. 22 Magnitude of time-averaged velocity for $\lambda = 6.0$ at $\theta = -60$ deg (f = 1120 Hz and U_{ave} = 7.0 m/s).

When $\theta = 0$ deg, $M_x = M$, and the momentum provides a large resistance to the vectoring of the primary jet because of its uptoward flow direction. The resistance caused by the momentum in the blowing stroke and vectoring effect of lower pressure near the synthetic jet finally balance each other and vector the primary jet at an approximately constant angle. This is also the reason why the vectoring angle of the primary jet does not always increase with larger velocity amplitude of the synthetic jet, as discussed before. Although higher velocity amplitude of the synthetic jet causes lower pressure region between the jets, it also results in larger momentum resistance to the vectoring of the primary jet.

When $\theta > 0$ deg, $M_y = M \sin\theta$ increases with larger θ, whereas $M_x = M\cos\theta$ decreases. As a result, the resistance effect of M_x is reduced, and M_y induces a vectoring velocity on the primary jet, which vectors the primary jet more. Thus the vectoring angle of the primary jet increases sharply with larger θ. With large enough velocity amplitude and angle of the synthetic jet (for example $\theta = 60$ deg), the primary jet can be totally attached to the wall.

When $\theta < 0$ deg, both the streamwise momentum component M_x and the cross-stream momentum component M_y induce resistance to the vectoring process because of its direction towards the primary jet, and their effects increase with larger $|\theta|$. With larger $|\theta|$ the lower pressure area between the two jets disappears gradually, and the resistance effect of the blowing stroke increases, making the primary jet vectored to the right. For example, at $\theta = -60$ deg, as shown in Fig. 22, the primary jet can be vectored to the right for reasonable values of parameters d_{pull}, f, U_{amp}, and U_{ave}.

Conclusions

In this study vectoring control of a primary jet with an averaged-zero-mass-flux synthetic jet is investigated using the two-dimensional Reynolds-averaged Navier–Stokes equations.

The numerical results show general agreement with the experiments of Smith and Glezer. Vectoring effects of the synthetic jet with different parameters, such as the location, oscillating frequency, velocity amplitude and angle, are studied in detail as the angle of the synthetic jet is 0 deg. In a certain range of the velocity of the primary jet, there exists an optimal value for the location, frequency, and velocity amplitude, respectively, where the largest vectoring angle of the primary jet is obtained with other parameters fixed.

When the angle of the synthetic jet is 60 deg, the vectoring angle of the primary jet can increase dramatically as the velocity amplitude of the synthetic jet increases, and the primary jet can finally attach to the wall. The optimal frequency for the largest vectoring angle also drops to a lower value at which a much larger vectoring angle can be obtained than that when the angle of the synthetic jet is zero. The simulations also show that when the angle of the synthetic jet is 60 deg a much larger vectoring force is obtained than that as it is 0 deg, with the same momentum input.

Finally, a hypothesis is provided to explain the vectoring process based on the simulations. It is suggested that the vectoring is mainly the combined effects of lower pressure near the exits of the jets and resistance caused by the momentum impulse of the synthetic jet in the blowing stroke. When the angle of the synthetic jet is bigger than zero, the resistance of the momentum impulse reduces as the angle increases, and therefore a larger vectoring angle of the primary jet can be obtained.

Acknowledgments

The authors thank Bart Smith of the Utah State University and Ari Glezer of the Georgia Institute of Technology for providing details of the experiments. This work was supported by a Boeing graduate fellowship.

References

[1] Smith, B. L., and Glezer, A., "The Formation and Evolution of Synthetic Jets," *Physics of Fluids*, Vol. 10, No. 9, 1998, pp. 2281–2297.

[2] Smith, B. L., and Glezer, A., "Vectoring and Small-Scale Motions Effected in Free Shear Flows Using Synthetic Jet Actuators," AIAA Paper 97-0213, Jan. 1997.

[3] Smith, B. L., Trautman, M. A., and Glezer, A., "Controlled Interactions of Adjacent Synthetic Jets," AIAA Paper 99-0669, Jan. 1999.

[4] Smith, D. R., Kibens, V., Parekh, D. E., and Glezer, A., "Thrust Vectoring with Hybrid Synthetic Jet Actuators," American Society of Mechanical Engineers, Paper FEDSM97-3679, June 1997.

[5] Ritchie, B. D., and Seitzman, J. M., "Acetone Mixing Control of Fuel Jets Using Synthetic Jet Technology: Scalar Field Measurements," AIAA Paper 99-0448, Jan. 1999.

[6] Rediniotis, O. K., Ko, J., and Yue, X., "Synthetic Jets, Their Reduced Order Modeling and Applications to Flow Control," AIAA Paper 99-1000, Jan. 1999.

[7] Pack, L. G., and Seifert, A., "Periodic Excitation for Jet Vectoring and Enhanced Spreading," AIAA Paper 99-0672, Jan. 1999.

[8] Miller, D. M., Yagle, P. J., and Hamstra, J. W., "Fluidic Throat Skewing for Thrust Vectoring in Fixed-Geometry Nozzles," AIAA Paper 99-0365, Jan. 1999.

[9] Raman, G., "Using Controlled Unsteady Fluid Mass Addition to Enhance Jet Mixing," *AIAA Journal*, Vol. 35, 1997, pp. 647–656.

[10] Strykowski, P. J., Krothapalli, A., and Forliti, D. J., "Counterflow Thrust Vectoring of Supersonic Jets," AIAA Paper 96-0115, Jan. 1996.

[11] Kral, L. D., Donovan, J. F., Cain, A. B., and Cary, A. W., "Numerical Simulation of Synthetic Jet Actuators," AIAA Paper 97-1824, June 1997.

[12] Kral, L. D., and Guo, D.-H., "Characterization of Jet Actuators for Active Flow Control," AIAA Paper 99-3573, June 1999.

[13] Guo, D.-H., Kral, L. D., and Cary, A. W., "Numerical Simulation of the Interaction of Adjacent Synthetic Jet Actuators," AIAA Paper 2000-2565, June 2000.

[14] Guo, D.-H., and Cary, A. W. "Vectoring Control of a Primary Jet with Synthetic Jets," AIAA Paper 2001-0738, Jan. 2001.

[15] Rogers, S. E., and Kwak, D., "An Upwind Differencing Scheme for the Time-Accurate Incompressible Navier–Stokes Equations," *AIAA Journal*, Vol. 28, No. 2, 1990, pp. 253–262.

[16] Rogers, S. E., Kwak, D., and Kiris, C., "Steady and Unsteady Solutions of the Incompressible Navier–Stokes Equations," *AIAA Journal*, Vol. 29, No. 4, 1991, pp. 603–610.

[17] Rogers, S. E., "A Comparison of Implicit Schemes for the Incompressible Navier–Stokes Equations with Artificial Compressibility," AIAA Paper 95-0567, Jan. 1995.

[18] Spalart, P. R., and Allmaras, S. R., "A One-Equation Turbulence Model for Aerodynamic Flows," AIAA Paper 92-0439, Jan. 1992.

[19] Smith, B. L., "Synthetic Jets and Their Interaction with Adjacent Jets," Ph.D. Dissertation, Dept. of Mechanical Engineering, Georgia Inst. of Technology, Atlanta, June 1999.

R. M. C. So
Associate Editor